Cryo-EM structures and binding of mouse ACE2 to SARS-CoV-2 variants of concern

Dongchun Ni[1], Priscilla Turelli[2], Bertrand Beckert[3], Sergey Nazarov[3], Emiko Uchikawa[3], Alexander Myasnikov[3], Florence Pojer[4], Didier Trono[2], Henning Stahlberg[1, $], Kelvin Lau[4,$]

[1] Laboratory of Biological Electron Microscopy (LBEM), Institute of Physics, School of Basic 15 Science, École Polytechnique Fédérale de Lausanne (EPFL), and Dep. of Fund. Microbiology, Faculty of Biology and Medicine, University of Lausanne, Lausanne, Switzerland

[2] Laboratory of Virology and Genetics (LVG), School of Life Sciences, École polytechnique fédérale de Lausanne (EPFL), Lausanne, Switzerland

[3]Dubochet Center for Imaging (DCI), École polytechnique fédérale de Lausanne (EPFL) and University of Lausanne, Lausanne, Switzerland

[4]Protein Production and Structure Characterization Core Facility (PTPSP), School of Life Sciences, École polytechnique fédérale de Lausanne (EPFL), Lausanne, Switzerland

[$] Corresponding authors: henning.stahlberg@epfl.ch, kelvin.lau@epfl.ch

ABSTRACT

Investigation of potential hosts of the severe acute respiratory syndrome coronavirus-2 (SARS-CoV-2) is crucial to understanding future risks of spillover and spillback. SARS-CoV-2 has been reported to be transmitted from humans to various animals after requiring relatively few mutations.[1] Mice are well adapted to human environments, frequently come in contact with humans, are used widely as infection models, and may act as reservoirs for SARS-CoV-2.[2] Structural and binding data of the mouse ACE2 receptor with the Spike protein of newly identified SARS-CoV-2 variants are needed to better understand the impact of variants of concern (VOC). Previous studies have developed mouse-adapted variants and have identified some determinants of binding.[3,4] Here we report the cryo-EM structures of mouse ACE2 bound to Spike ectodomains of four different VOC: Beta, Omicron BA.1, Omicron BA.2.12.1 and Omicron BA.4/5. These variants represent the oldest to the newest variants that are able to bind the mouse ACE2 receptor. Our high-resolution structural data

29 complemented with bio-layer interferometry (BLI) binding assays reveal a requirement for a
30 combination of mutations in the Spike protein to enable the binding to mouse ACE2.
31
32 We performed BLI binding assays between SARS-CoV2 variants of concern to characterize
33 the binding affinities of dimeric mouse ACE2 (mACE2) compared to that of the human
34 receptor (hACE2). The wild-type Spike protein bound robustly hACE2 but not strongly to
35 mACE2, with only appreciable signal at the highest concentration of 300 nM (Supplementary
36 information, Fig. S1). With the emergence of the first generation of SARS-CoV2 variants,
37 Alpha, Beta and Gamma, all sharing the N501Y mutation in their Spike protein
38 (Supplementary information, Fig. S2), it was reported that mice were susceptible to
39 infection.[5–7] We observed an increase in affinity to the mACE2 where we could detect
40 appreciable binding with dissociation constants (K_d) measuring below 100 nM as compared
41 to wild-type (Fig. 1a, Supplementary information, Fig. S1). mACE2 increased its affinity for
42 Spike further with the appearance with Omicron BA.1 and BA.2 with up to 10-fold increase
43 compared to wild-type (Fig. 1a, Supplementary information, Fig. S1). The Spike protein from
44 more recent Omicron BA.2.12.1 and BA.4/5 variants, containing additional mutations, still
45 bound strongly to the receptor binding domain (RBD) interface (Fig. 1a, Supplementary
46 information, Fig. S2). To probe how variants of concern gained high affinity mACE2
47 binding, utilizing cryo-EM, we determined the structures of four mACE2/Spike VOC
48 complexes spanning the variants Beta, Omicron BA.1, BA.2.12.1, and BA.4/5, at resolutions
49 of 3.9 Å, 2.7Å, 2.9 Å and 2.9Å, respectively (Fig. 1b and Supplementary information, Figs.
50 S3-S7). We also solved the hACE2/BA.4/5 Spike complex at 2.8Å for comparison
51 (Supplementary information, Fig. S7). All of the structures show that mACE2/hACE2 bind
52 the RBD of the Spike protein in the same manner at the binding ridge of a RBD in the up-
53 position. During cryo-EM data-processing we observed the RBD of all Spikes in either a 2-up
54 or 3-up conformation, with each up-RBD having an ACE2 bound (Supplementary
55 information, Figs. S3-S7). To gain structural information at side-chain level resolution of the
56 binding interface, we performed image processing of the cryo-EM data by location-focused
57 refinement. This yielded maps at higher quality for each variant's ACE2/RBD interface,
58 allowing to better understand the effects of mutations in these regions (Fig. 1c,
59 Supplementary information, Figs. S3-S8).
60
61 SARS-CoV2 variants Alpha, Beta and Gamma the first reported to be able to engage
62 mACE2, and all share a crucial N501Y mutation in their Spike proteins. In the mACE2/Beta

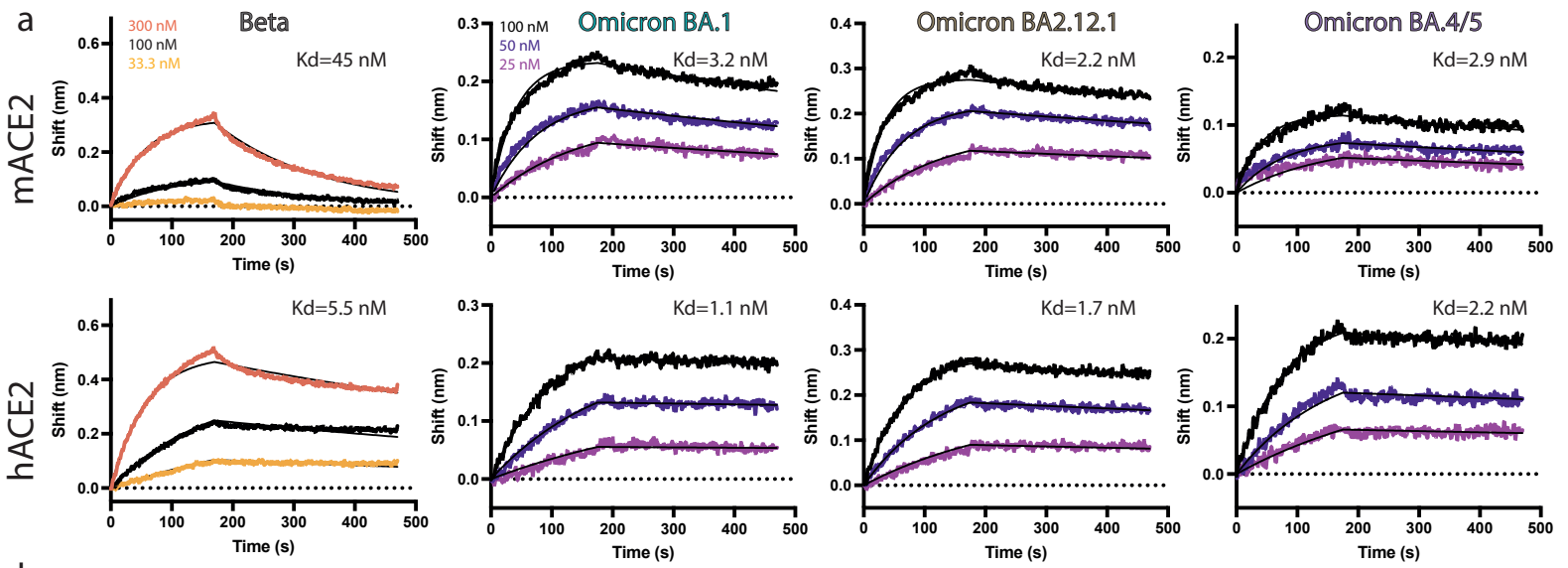

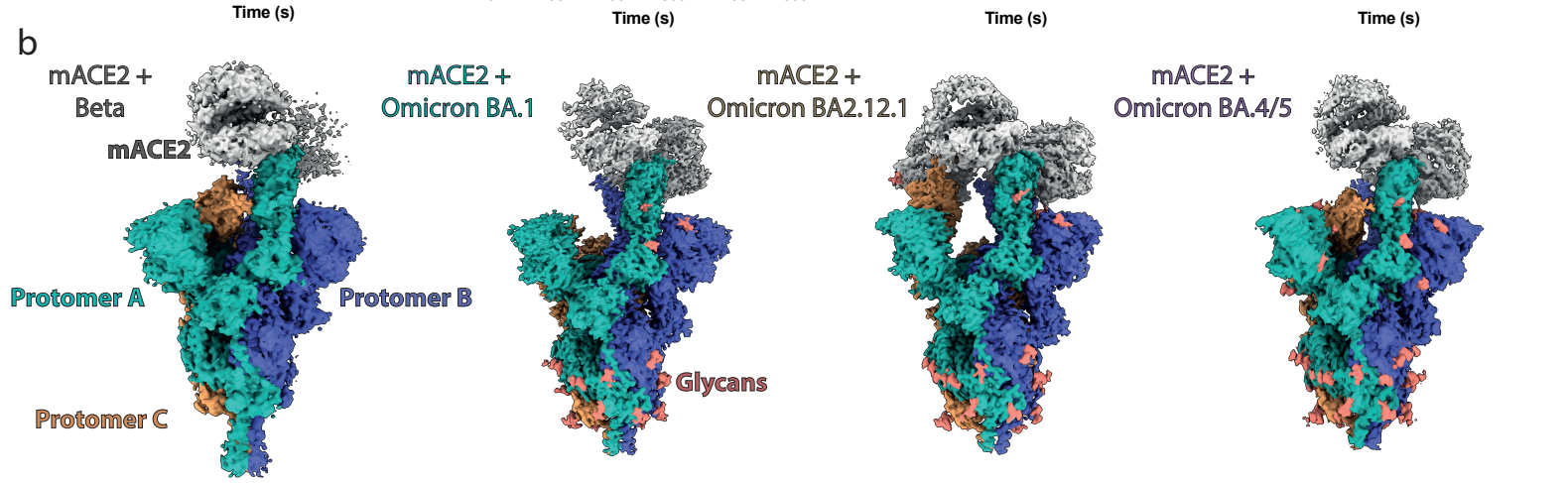

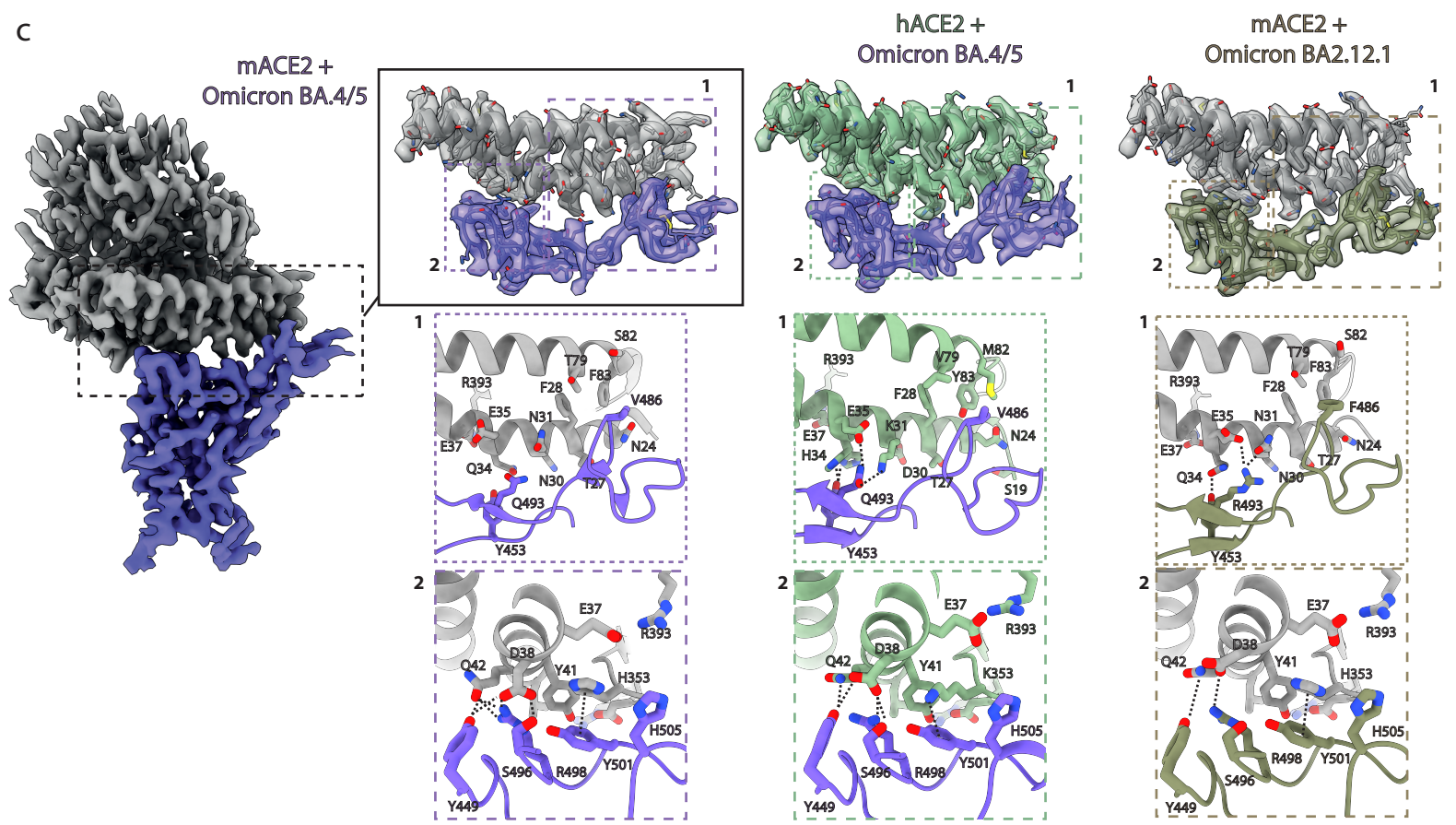

d

	19	24	27	28	30	31	34	35	37	38	41	42	45	79	82	83	330	353	355	357	393
human	S	Q	T	F	D	K	H	E	E	D	Y	Q	L	L	M	Y	N	K	D	R	R
mouse	S	N	T	F	N	N	Q	E	E	D	Y	Q	L	T	S	F	N	H	D	R	R
hamster	S	Q	T	F	D	K	Q	E	E	D	Y	Q	L	L	N	Y	N	K	D	R	R
cat	S	L	T	F	E	K	H	E	E	E	Y	Q	L	L	T	Y	N	K	D	R	R
dog	–	L	T	F	E	K	Y	E	E	E	Y	Q	L	L	T	Y	N	K	D	R	R
mink	S	L	T	F	E	K	Y	E	E	E	Y	Q	L	H	T	Y	N	K	D	R	R

Figure 1

structure, we observe that the Spike N501Y mutation, which replaces a polar asparagine (N) residue with a polar and aromatic tyrosine (Y) residue, allows for π-π interactions with Y43 of mACE2, and potentially enables a new cation-π and hydrogen bond interaction with the histidine H353, which is unique to the mouse mACE2 (Supplementary information, Fig. S9). This crucial Spike Y501 is also present in all later identified Omicron Spike variants. Beta and Gamma also share E484K and K417N/T as signature mutations in the Spike's RBD (Supplementary information, Fig S2). These two residues are unfortunately not resolved in our cryo-EM maps. However, *in vitro* BLI experiments showed that alongside N501Y, the E484K mutation can confer high-affinity binding of the Spike to mACE2 (Supplementary information, Fig. S1). We could not observe any binding of single mutants of N501Y, E484K or K417N of the Spike protein to mACE2. Only the combined presence of Y501 and K484 in the Spike protein showed binding to mACE2 at the concentration of Spike protein tested here (75 nM).

We next investigated Omicron variants BA.1, BA.2, BA.2.12.1 and BA.4/5 that most recently caused new waves of infections in several countries during the year 2022.[8,9] These variants contain up to 34 mutations scattered across the entire Spike protein, with the majority concentrated on the RBD, including N501Y and E484A (Supplementary information, Fig. S2). The accumulation of these mutations prompted an ongoing discussion about a possible murine origin of the Omicron variant.[10] Indeed, our here presented mACE2/BA.1 structure reveals multiple new interactions localized in two different patches. In patch 1, the longer arginine (R) sidechain of the BA.1 RBD Q493R mutation allows for hydrogen bonding with mACE2 residues N31 and Q34, which was not possible with the shorter glutamine (Q) residue present in the original Spike protein (Supplementary information, Fig. S9). In patch 2, Y501 is observed to form cation-π interactions with H353 from mACE2, and new BA.1 mutations G496S and Q498R form a new set of hydrogen-bonds and electrostatic interactions with mACE2's aspartic acid D38 (Supplementary information, Fig. S9). Overall, Omicron BA.1 mutations Q493R and Q498R are crucial for stronger binding to mACE2, alongside with the N501Y and E484A/K mutations present in preceding variants. These new interactions greatly increase the binding between mACE2 and Omicron Spike proteins with measured affinities by BLI up to 14-20-fold stronger compared to Beta (Fig. 1 and Supplementary information, Fig. S1).

Both the BA.2.12.1 and BA.4/5 Omicron subvariants carry the immune-evading L452R mutation first seen in the Delta variant. The site of mutation is not within the RBD-ACE2 binding interface and, as expected, the binding affinities for both hACE2 and mACE2 binding to BA.2.12.1 are unchanged compared to BA.2 (Fig. 1a, Supplementary information, Fig. S1). In the mACE2/BA.2.12.1 structure, the critical interactions made by Spike residues R498 and Y501 with mACE2 within patch 2 are conserved as in BA.1 (Fig. 1c). Interestingly, R493 of BA.2.12.1 has an alternative hydrogen bonding network with N31 and E35, instead of Q34, which now forms a hydrogen bond with Y453 of mACE2 suggesting a plasticity in its interactions (Fig. 1c).

The Omicron subvariants BA.4 and BA.5 that were the principal variants during an infection wave in the summer of 2022, share the L452R mutation. In addition, BA.4 and BA.5 contain the F486V mutation, and the reversion of R493 back to the wild-type Q493 (Supplementary information, Fig. S2). The structure the mACE2/BA.4/5 complex show crucial changes at patch 1, where the BA.4/5 mutation F486V loses Van der Waals interactions with adjacent mACE2 residues F83 and F28, and the wild-type Q493 (R493Q wild-type reversion) on the Spike's RBD no longer forms interactions with mACE2 (Fig. 1c). The hACE2/BA.4/5 structures reveal the same loss of interactions for the Spike's F486V mutation, but the Spike's Q498 once again allows for an interaction to be formed with hACE2's K31, which was not possible with the Spike's R498 due to its charge repulsion from hACE's K31 (Fig. 1c). The two mutations together allow for BA.4/5 Spike to maintain high affinity interactions with both, hACE2 and mACE2. This is an example of the interplay between balancing immune evasion, while maintaining high-affinity receptor binding. The other principal interactions between mACE2 and Spike's BA.4/5 in patch 2 are comparable to those observed between mACE2 and variants BA.1 or BA2.12.1.

In summary, our structural data and binding analysis of mACE2 to SARS-CoV-2 variants of concern highlight the evolutionary adaptations that have allowed the virus to evade the human immune system, and how those mutations impacted receptor binding in mice. Our results identified critical mutations of SARS-CoV-2's Spike protein, N501Y, E484K, Q493R and Q498R, that are required for high-affinity binding to mACE2, contributing a structural basis for our understanding of the potential of spillback of SARS-CoV-2 into the animal kingdom.

FIGURE LEGENDS

Fig. 1: Structural basis for mACE2 binding to Omicron variants of concern. **a** BLI binding assays of captured dimeric mouse or human ACE2 versus various concentrations of Spike variants of concern. Data curves are colored by concentration and the black line indicates the 1:1 fit of the data. **b** Cryo-EM densities of the full mACE2/Spike variant of concern complexes. Each protomer of the Spike trimer is colored separately with mACE2 colored in grey. **c** Focused refinement of the RBD-ACE2 interface of the mACE2 BA.4/5 complex showing the cryo-EM density. Inset shows the zoomed view of the binding interface. The same view is shown for the hACE2/BA.4/5 and mACE2/BA2.12.1 complexes. **d** Zoomed views of specific interaction sites of patch 1 and patch 2 as indicated in (**c**). **e** Sequence alignment of human ACE2 with mouse ACE2 and other selected species. Red boxes highlight critical differences between human and mouse ACE2 residues.

DATA AVAILABILITY

Cryo-EM maps for the Spike variants in complex with mouse ACE2 were deposited in the Electron Microscopy Data Bank (EMDB) under the access codes EMD-15541 (full map, Beta, two mACE2 bound), EMD-15589 (local map, mACE2/Beta), EMD- 15580 (full map, BA.1, two mACE2 bound), EMD-15581 (full map, BA.1, three mACE2 bound), EMD-15590 (local map, mACE2/BA.1), EMD-15584 (full map, BA.2.12.1, two mACE2 bound), EMD-15585 (full map, BA2.12.1, three mACE2 bound), EMD-15591 (local map, mACE2/BA.2.12.1), EMD-15586 (full map, BA.4/5, two mACE2 bound) and EMD-15592 (local map, mACE2/BA.4/5).

Maps for Spike the human ACE2/Omicron BA.4/5 complex were deposited in the EMDB under the access codes EMD-15587 (full map, BA.4/5, three hACE2 bound) and EMD-15588 (local map, hACE2/BA.4/5).

Atomic models were deposited in Protein Data Bank (PDB) under the access codes of PDB-8AQS (hACE2-BA.4/5), PDB-8AQT (mACE2/Beta), PDB-8AQU (mACE2/BA.1), PDB-8AQV (mACE2/BA.2.12.1) and PDB-8AQW (mACE2/BA.4/5).

Raw electron microscopy image data were deposited at the Electron Microscopy Public Image Archive (EMPIAR) under access codes EMPIAR-XXXXX (Beta, two mACE2 bound), EMPIAR-XXXXX (BA.1, two mACE2 bound), EMPIAR-XXXXX (BA.1, three

mACE2 bound), EMPIAR-XXXXX (BA.2.12.1, two mACE2 bound), EMPIAR-XXXXX (BA2.12.1, three mACE2 bound), and EMPIAR-XXXXX (BA.4/5, two mACE2 bound).

CONTRIBUTIONS

D.N., K.L., P.T., F.P., D.T. designed the project. P.T. designed and cloned the Spike variants. K.L purified the Omicron Spike and ACE2 and performed BLI assays. B.B., S.N., E.U., A.M., froze and screened cryo-EM grids, collected data, and performed on-the-fly processing. D.N. processed cryo-EM data and built models. D.N. and K.L. analyzed data and prepared figures. K.L., D.N., wrote the manuscript. F.P., H.S., and D.T. supervised the project.

ACKNOWLEDGEMENTS

Cryo-EM data collection and initial image processing was performed at the Dubochet Center for Imaging, a common initiative of the EPFL, UNIL and UNIGE, with data collection performed in both Geneva and Lausanne. We thank Yashar Sadian for data collection on the Talos Arctica. We thank Rosa Schier, Laurence Durrer, Soraya Quinche and Michael François of the Protein Production and Structure Core Facility of EPFL for helping in the production of Spike Omicron and ACE2. Charlene Raclot for cloning of the Spike variants. This work was supported in part by NCCR TransCure, a National Centre of Competence in Research, funded by the Swiss National Science Foundation (grant number 185544)

REFERENCES

1. Tan, C. C. S. *et al.* Transmission of SARS-CoV-2 from humans to animals and potential host adaptation. *Nat Commun* **13**, 2988 (2022).
2. Muñoz-Fontela, C. *et al.* Advances and gaps in SARS-CoV-2 infection models. *PLOS Pathogens* **18**, e1010161 (2022).
3. Sun, S. *et al.* Characterization and structural basis of a lethal mouse-adapted SARS-CoV-2. *Nat Commun* **12**, 5654 (2021).
4. Dinnon, K. H. *et al.* A mouse-adapted model of SARS-CoV-2 to test COVID-19 countermeasures. *Nature* **586**, 560–566 (2020).

194 5. Yao, W. *et al.* Circulating SARS-CoV-2 variants B.1.1.7, 501Y.V2, and P.1 have gained
195 ability to utilize rat and mouse Ace2 and altered in vitro sensitivity to neutralizing
196 antibodies and ACE2-Ig. *bioRxiv* 2021.01.27.428353 (2021)
197 doi:10.1101/2021.01.27.428353.
198 6. Thakur, N. *et al.* SARS-CoV-2 variants of concern alpha, beta, gamma and delta have
199 extended ACE2 receptor host ranges. *Journal of General Virology* **103**, 001735.
200 7. Montagutelli, X. *et al. The B1.351 and P.1 variants extend SARS-CoV-2 host range to*
201 *mice*. http://biorxiv.org/lookup/doi/10.1101/2021.03.18.436013 (2021)
202 doi:10.1101/2021.03.18.436013.
203 8. Viana, R. *et al. Rapid epidemic expansion of the SARS-CoV-2 Omicron variant in*
204 *southern Africa*. 2021.12.19.21268028
205 https://www.medrxiv.org/content/10.1101/2021.12.19.21268028v1 (2021)
206 doi:10.1101/2021.12.19.21268028.
207 9. Tegally, H. *et al.* Emergence of SARS-CoV-2 Omicron lineages BA.4 and BA.5 in South
208 Africa. *Nat Med* 1–6 (2022) doi:10.1038/s41591-022-01911-2.
209 10. Wei, C. *et al.* Evidence for a mouse origin of the SARS-CoV-2 Omicron variant. *Journal*
210 *of Genetics and Genomics* (2021) doi:10.1016/j.jgg.2021.12.003.
211 11. Punjani, A., Rubinstein, J. L., Fleet, D. J. & Brubaker, M. A. cryoSPARC: algorithms for
212 rapid unsupervised cryo-EM structure determination. *Nat Methods* **14**, 290–296 (2017).
213 12. Pettersen, E. F. *et al.* UCSF Chimera—A visualization system for exploratory research
214 and analysis. *Journal of Computational Chemistry* **25**, 1605–1612 (2004).
215 13. Emsley, P., Lohkamp, B., Scott, W. G. & Cowtan, K. Features and development of Coot.
216 *Acta Cryst D* **66**, 486–501 (2010).
217 14. Liebschner, D. *et al.* Macromolecular structure determination using X-rays, neutrons and
218 electrons: recent developments in Phenix. *Acta Cryst D* **75**, 861–877 (2019).

15. Pettersen, E. F. *et al.* UCSF ChimeraX: Structure visualization for researchers, educators, and developers. *Protein Science* **30**, 70–82 (2021).

Supplementary Information

METHODS AND MATERIALS

Protein Production and Purification

The Spike trimer was designed to mimic the native trimeric conformation of the protein in vivo and the expression vector was kindly provided by Prof. Jason McLellan, University of Texas, Austin (TX), USA. It encoded the prefusion ectodomain of the original 2019-CoV Spike, containing a native signal peptide, residues 986 and 987 mutated to proline (2P), a mutated putative furin cleavage site (residues 682-685 mutated to GSAS), a C-terminal T4 foldon fusion domain to stabilize the trimer complex, followed by C-terminal 8x His and 2x Strep tags for affinity purification. The trimeric Spike protein was transiently expressed in suspension-adapted ExpiCHO cells (Thermo Fisher) in ProCHO5 medium (Lonza) at 5 x10^6 cells/mL using PEI MAX (Polysciences) for DNA delivery. At 1 h post-transfection, dimethyl sulfoxide (DMSO; AppliChem) was added to 2% (v/v). Following a 7-day incubation with agitation at 31 °C and 4.5% CO_2, the cell culture medium was harvested and clarified using a 0.22 µm filter. The conditioned medium was loaded onto Streptactin XT columns (IBA) washed with PBS and eluted with 50 mM biotin in 150 mM NaCl, 100 mM HEPES 7.5. Eluted protein was then dialyzed overnight into PBS. The purity of Spike trimers was determined to be >99% pure by SDS-PAGE analysis. Point mutations were generated by InFusion-mediated site directed mutagenesis. Variant clones were generated by gene synthesis (Twist Biosciences, Genscript and IDT) on the 2019-CoV Spike background as above. All mutants were produced and purified in an identical manner to the original 2019-Cov S protein.

Cryo-electron microscopy

mACE2/Beta complex

Cryo-EM grids were prepared with a Leica EM GP2 (Leica) plunge-freezing device, using Quantifoil R2/1 copper 400 grids. 3.0 µL of a sample containing 0.4 µM Beta Spike and 0.7 µM mACE2-Fc was applied to the glow-discharged grids, and backblotted for 2 s with a 10 s

251 wait time, 80% humidity and 10 °C in the sample chamber, and the blotted grids were
252 plunge-frozen in liquid nitrogen-cooled liquid ethane.
253
254 Grids were screened for particle presence and ice quality on a TFS Talos Arctica transmission
255 electron microscope (TEM) operated at 200kV. Cryo-EM data was collected using the same
256 microscope, equipped with a TFS Falcon 3 camera. Movies were recorded at a nominal
257 magnification of 150kx, corresponding to a 0.9759Å pixel, with defocus values ranging from
258 -0.8 to -2.5 µm. Exposures were adjusted automatically to 40 e-/Å2 total dose with automatic
259 collection using EPU.
260
261 **mACE2/Omicron BA.1 complex**
262 Cryo-EM grids were prepared with a Vitrobot Mark IV (Thermofisher Scientific (TFS)).
263 Quantifoil R1.2/1.3 Au 400 holey carbon grids were glow-discharged for 120 s at 15mA
264 using a PELCO easiGlow device (Ted Pella, Inc.). 3.0 µL of a sample containing 9 µM
265 Omicron BA.1 and 16 µM mACE-Fc was applied to the glow-discharged grids, and blotted
266 for 6 s under blot force 10 at 100% humidity and 4 °C in the sample chamber, and the blotted
267 grids were plunge-frozen in liquid nitrogen-cooled liquid ethane.
268
269 Grids were screened for particle presence and ice quality on a TFS Glacios TEM (200kV),
270 and the best grids were transferred to TFS Titan Krios G4 TEM. Cryo-EM data was collected
271 using TFS Titan Krios G4, equipped with a Cold-FEG and Selectris X energy filter, on a
272 Falcon IV detector in electron counting mode. Falcon IV gain references were collected just
273 before data collection. Data was collected using TFS EPU v2.12.1 using aberration-free
274 image shift protocol (AFIS). Movies were recorded at the nominal magnification of 165kx,
275 corresponding to the 0.726Å pixel size at the specimen level, with defocus values ranging
276 from -0.7 to -2.0 µm. Exposures were adjusted automatically to 60 e-/$Å^2$ total dose.
277
278 **hACE2/Omicron BA.4/5, mACE2/Omicron BA.4/5, mACE2/Omicron BA.2.12.1**
279
280 Cryo-EM grids were prepared with a Vitrobot Mark IV (Thermofisher Scientific (TFS)).
281 Quantifoil R1.2/1.3 Au 400 holey carbon grids were glow-discharged for 120 s at 15mA
282 using a PELCO easiGlow device (Ted Pella, Inc.). 3.0 µL of a sample containing 14 µM of
283 the corresponding Spike and 25 µM mACE-Fc was applied to the glow-discharged grids, and

284 blotted for 6 s under blot force 10 at 100% humidity and 4 °C in the sample chamber, and the
285 blotted grid was plunge-frozen in liquid nitrogen-cooled liquid ethane.
286
287 Grids were screened for particle presence and ice quality on a TFS Glacios TEM (200kV),
288 and the best grids were transferred to TFS Titan Krios G4 TEM. Cryo-EM data was collected
289 using the TFS Titan Krios G4 TEM, equipped with a Cold-FEG, on a Falcon IV detector in
290 electron counting mode. Falcon IV gain references were collected just before data collection.
291 Data was collected using TFS EPU v2.12.1 using aberration-free image shift protocol (AFIS).
292 Movies were recorded at nominal magnification of 165kx, corresponding to the 0.83Å pixel
293 size at the specimen level, with defocus values ranging from -0.7 to -2.5 µm. Exposures were
294 adjusted automatically to 60 e-/Å2 total dose.
295
296 **Cryo-EM image processing**
297 On-the-fly processing was first performed during data acquisition for evaluating the data
298 quality during screening by using cryoSPARC live v3.3.1.4.[11] The obtained ab-initio
299 structures were used as templates for better particle picking. Motion correction was
300 performed on raw stacks without binning, using the cryoSPARC implementation of motion
301 correction. The full data processing workflow is shown in Supplementary information, Figs.
302 S3-S8 and processing statistics on Table 1.
303
304 **Cryo-electron microscopy model building**
305 The models of a SARS-CoV2 Spike (PDB ID 7QO7), mouse ACE2 (PDB ID 7FDK) and
306 human ACE2 (PDB ID 7FDG) were re-fit into the cryo-EM maps with UCSF Chimera.[12]
307 These docked models were extended and rebuilt manually with refinement, using Coot and
308 Phenix.[13,14] Figures were prepared in UCSF ChimeraX.[15]
309
310 **Biolayer Interferometry (BLI)**
311 All experiments were performed on a Gator BLI system. Running buffer was 150 mM NaCl,
312 10 mM HEPES 7.5. For binding assays, dimeric Fc-ACE2 was diluted to 10 µg/mL and
313 captured with MFc tips (GatorBio). Loaded tips were dipped into a 3 or 2-fold serial dilution
314 series (300 nM, 100 nM, 33.3 nM, or 100 nM, 50 nM, 25 nM) of target analyte Spike protein.
315 Screening of independent point mutations was done as above at a single concentration of 75
316 nM. Curves were processed using the Gator software with a 1:1 fit after background
317 subtraction. Plots were generated in Prism 9.

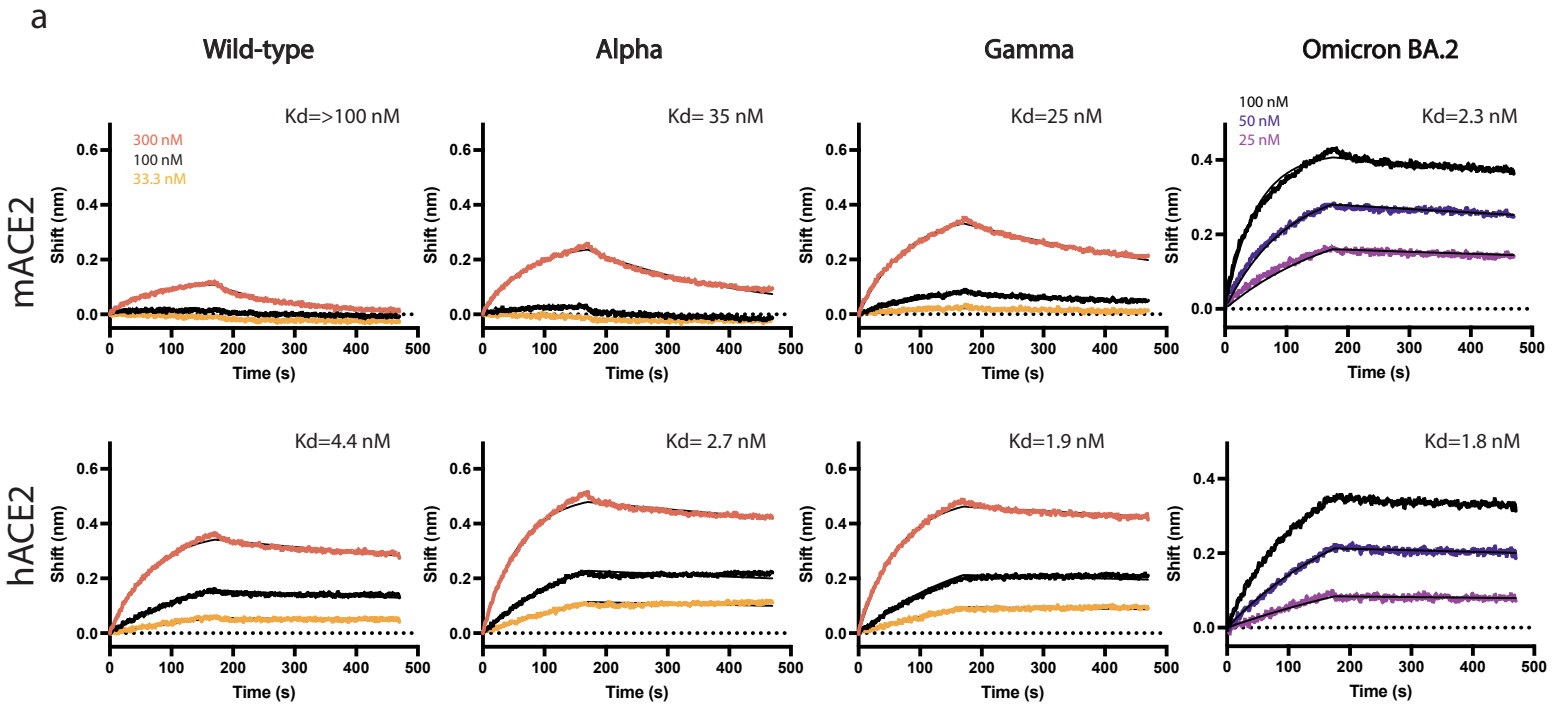
a
Wild-type
Alpha
Gamma
Omicron BA.2
mACE2
hACE2
Kd=>100 nM
Kd= 35 nM
Kd=25 nM
Kd=2.3 nM
Kd=4.4 nM
Kd= 2.7 nM
Kd=1.9 nM
Kd=1.8 nM
300 nM
100 nM
33.3 nM
100 nM
50 nM
25 nM
Shift (nm)
Time (s)

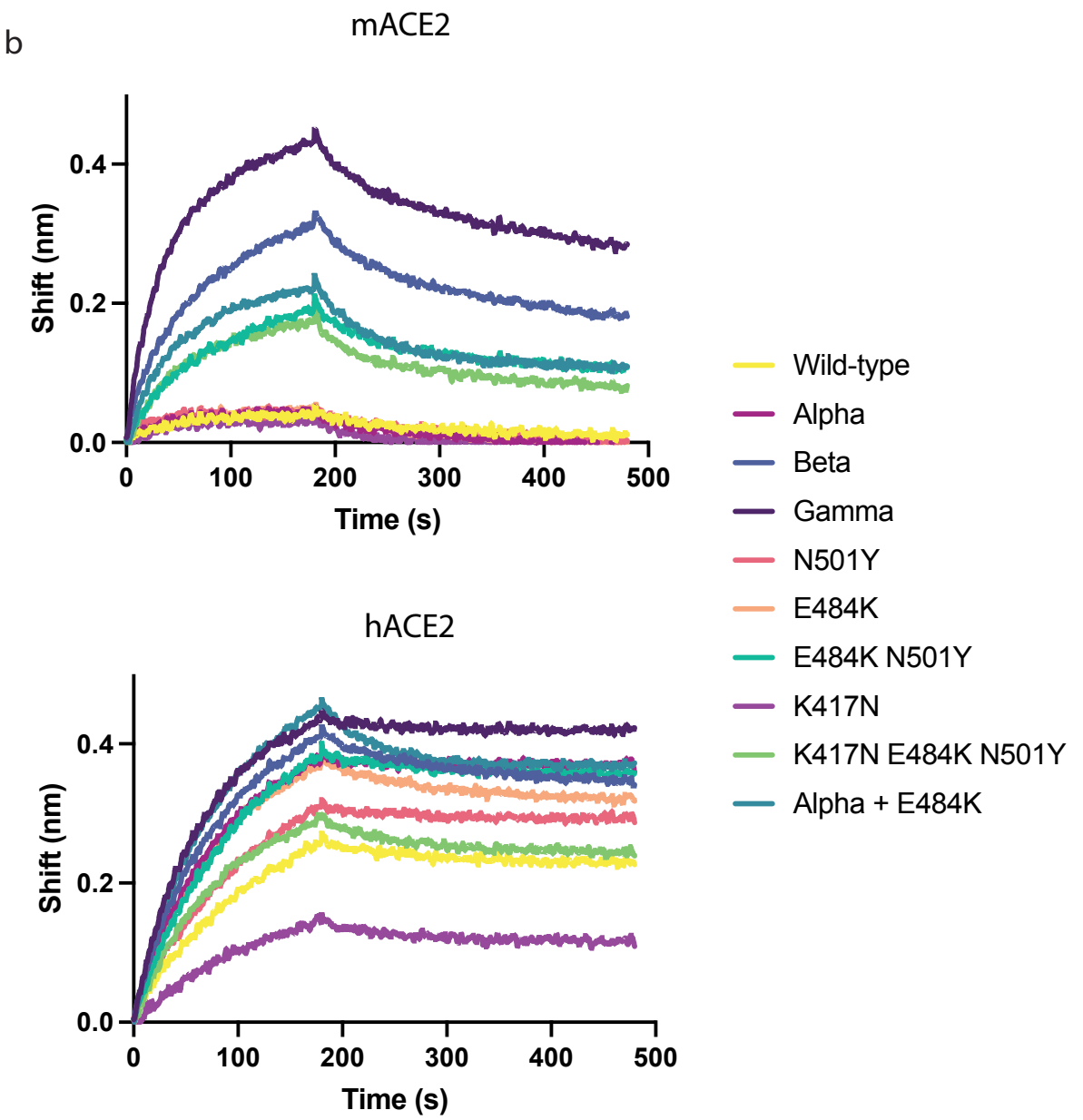
b
mACE2
hACE2
Shift (nm)
Time (s)
Wild-type
Alpha
Beta
Gamma
N501Y
E484K
E484K N501Y
K417N
K417N E484K N501Y
Alpha + E484K

Figure S1

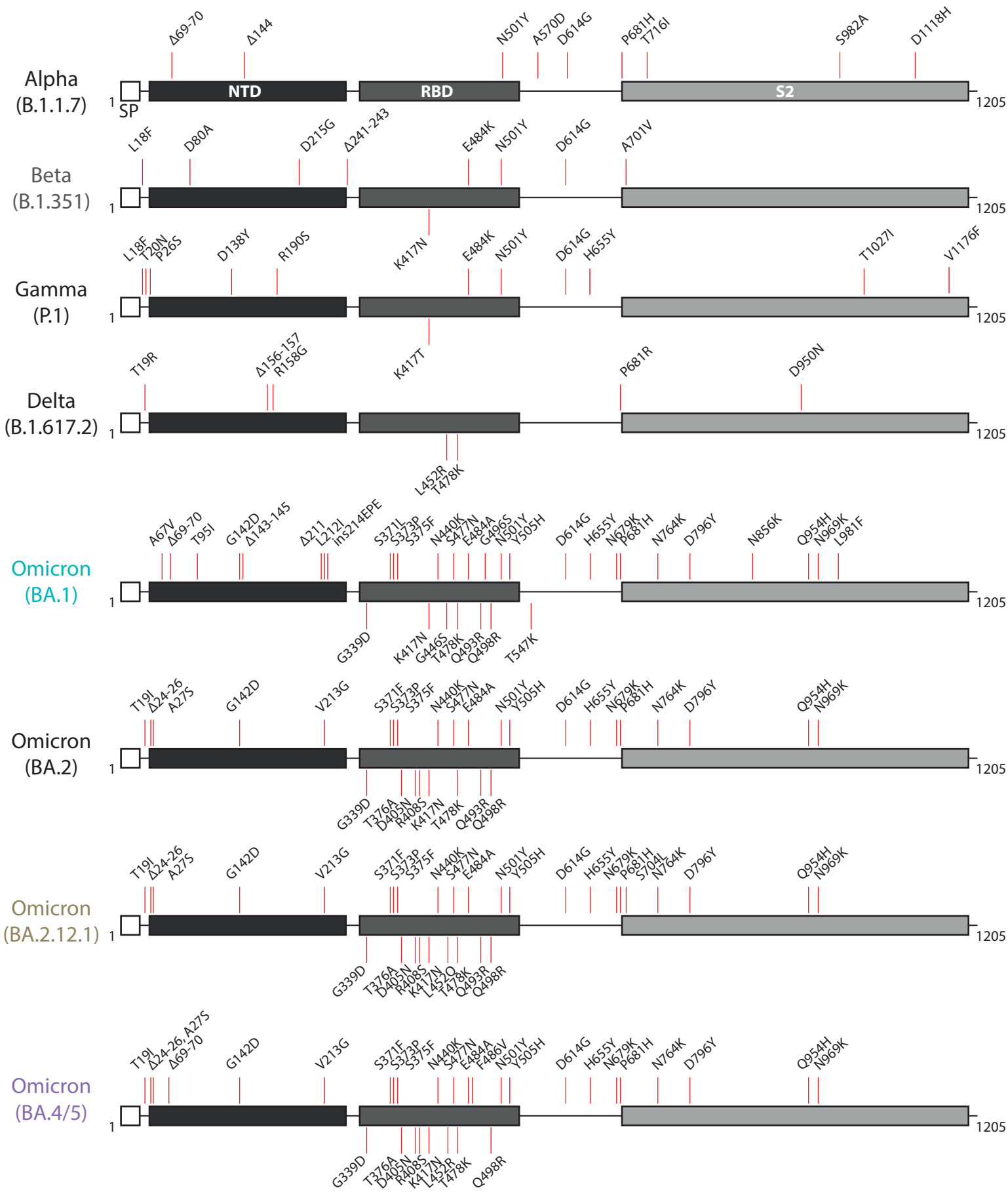
Alpha
(B.1.1.7)
Δ69-70
Δ144
N501Y
A570D
D614G
P681H
T716I
S982A
D1118H
1
SP
NTD
RBD
S2
1205
Beta
(B.1.351)
L18F
D80A
D215G
Δ241-243
E484K
N501Y
D614G
A701V
K417N
Gamma
(P.1)
L18F
T20N
P26S
D138Y
R190S
K417N
E484K
N501Y
D614G
H655Y
T1027I
V1176F
Delta
(B.1.617.2)
T19R
Δ156-157
R158G
K417T
P681R
D950N
L452R
T478K
Omicron
(BA.1)
A67V
Δ69-70
T95I
G142D
Δ143-145
Δ211
L212I
ins214EPE
S371L
S373P
S375F
N440K
S477N
E484A
G496S
N501Y
Y505H
D614G
H655Y
N679K
P681H
N764K
D796Y
N856K
Q954H
N969K
L981F
G339D
K417N
G446S
T478K
Q493R
Q498R
T547K
Omicron
(BA.2)
T19I
Δ24-26
A27S
G142D
V213G
S371F
S373P
S375F
N440K
S477N
E484A
N501Y
Y505H
D614G
H655Y
N679K
P681H
N764K
D796Y
Q954H
N969K
G339D
T376A
D405N
R408S
K417N
T478K
Q493R
Q498R
Omicron
(BA.2.12.1)
T19I
Δ24-26
A27S
G142D
V213G
S371F
S373P
S375F
N440K
S477N
E484A
N501Y
Y505H
D614G
H655Y
N679K
P681H
S704L
N764K
D796Y
Q954H
N969K
G339D
T376A
D405N
R408S
K417N
L452Q
T478K
Q493R
Q498R
Omicron
(BA.4/5)
T19I
Δ24-26
A27S
Δ69-70
G142D
V213G
S371F
S373P
S375F
N440K
S477N
E484A
F486V
N501Y
Y505H
D614G
H655Y
N679K
P681H
N764K
D796Y
Q954H
N969K
G339D
T376A
D405N
R408S
K417N
L452R
T478K
Q498R

Figure S2

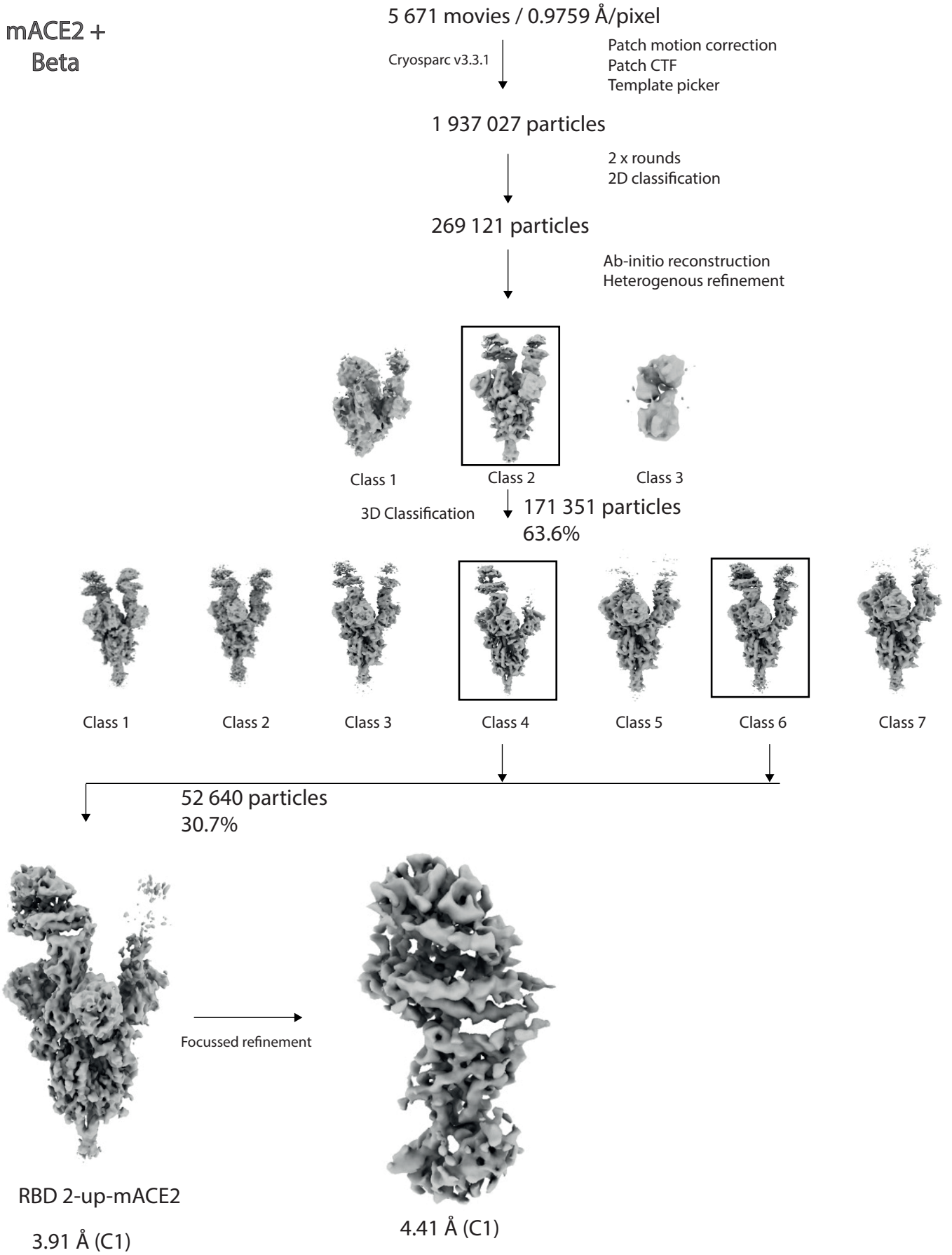
mACE2 +
Beta
5 671 movies / 0.9759 Å/pixel
Cryosparc v3.3.1
Patch motion correction
Patch CTF
Template picker
1 937 027 particles
2 x rounds
2D classification
269 121 particles
Ab-initio reconstruction
Heterogenous refinement
Class 1
Class 2
Class 3
3D Classification
171 351 particles
63.6%
Class 1
Class 2
Class 3
Class 4
Class 5
Class 6
Class 7
52 640 particles
30.7%
Focussed refinement
RBD 2-up-mACE2
3.91 Å (C1)
4.41 Å (C1)

Figure S3

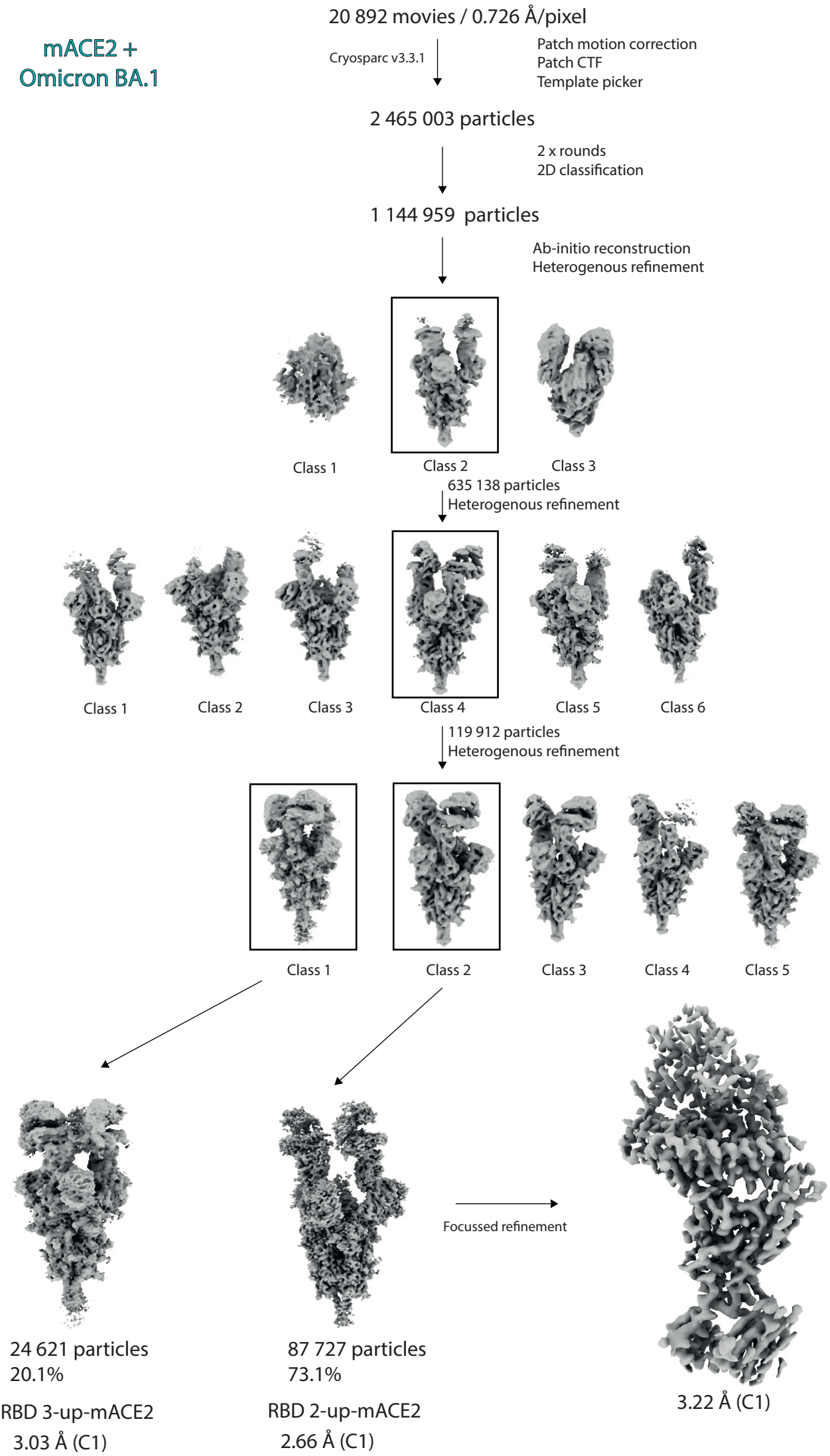
mACE2 +
Omicron BA.1
20 892 movies / 0.726 Å/pixel
Cryosparc v3.3.1
Patch motion correction
Patch CTF
Template picker
2 465 003 particles
2 x rounds
2D classification
1 144 959 particles
Ab-initio reconstruction
Heterogenous refinement
Class 1
Class 2
Class 3
635 138 particles
Heterogenous refinement
Class 1
Class 2
Class 3
Class 4
Class 5
Class 6
119 912 particles
Heterogenous refinement
Class 1
Class 2
Class 3
Class 4
Class 5
Focussed refinement
24 621 particles
20.1%
RBD 3-up-mACE2
3.03 Å (C1)
87 727 particles
73.1%
RBD 2-up-mACE2
2.66 Å (C1)
3.22 Å (C1)

Figure S4

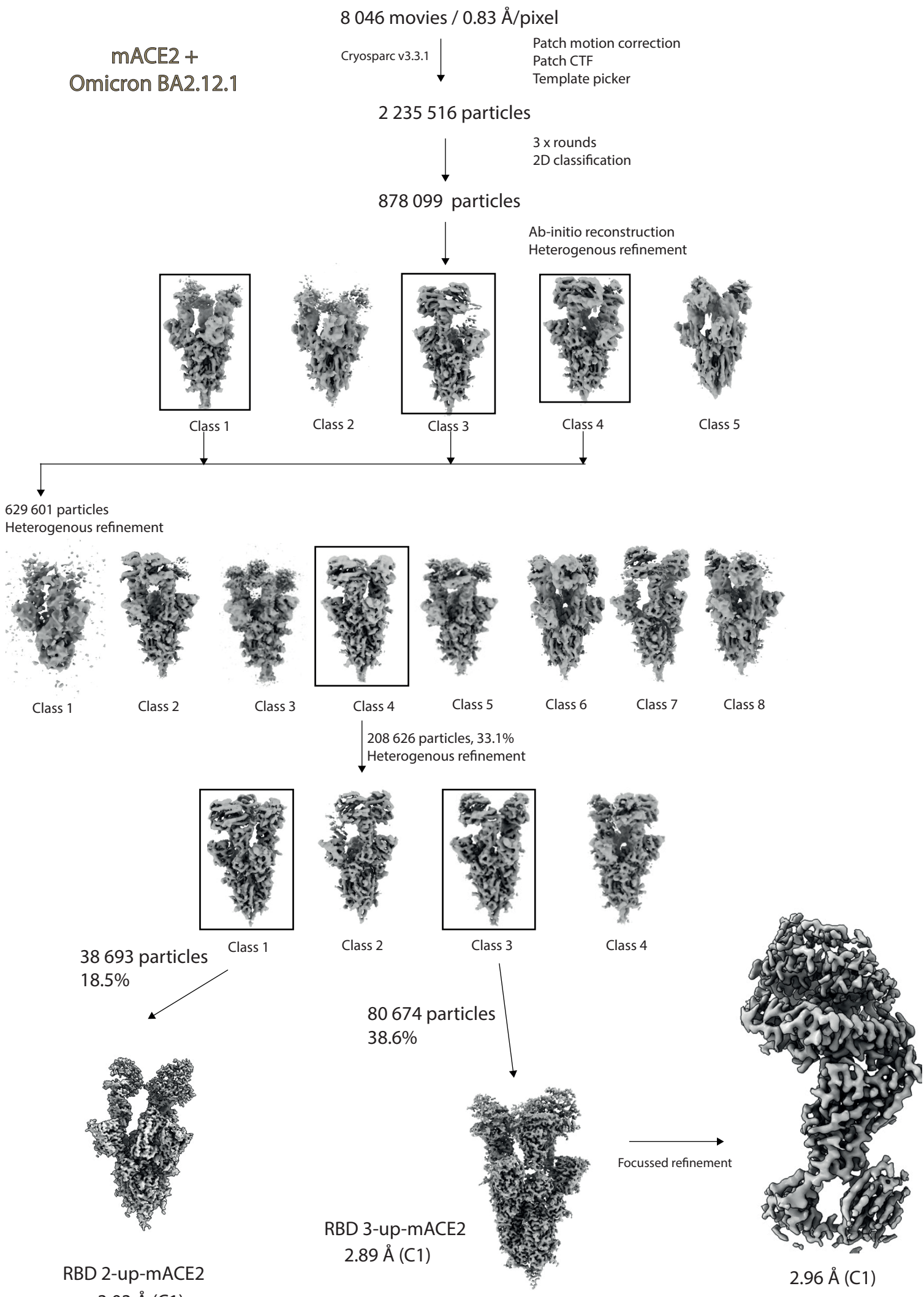
mACE2 +
Omicron BA2.12.1
8 046 movies / 0.83 Å/pixel
Cryosparc v3.3.1
Patch motion correction
Patch CTF
Template picker
2 235 516 particles
3 x rounds
2D classification
878 099 particles
Ab-initio reconstruction
Heterogenous refinement
Class 1
Class 2
Class 3
Class 4
Class 5
629 601 particles
Heterogenous refinement
Class 1
Class 2
Class 3
Class 4
Class 5
Class 6
Class 7
Class 8
208 626 particles, 33.1%
Heterogenous refinement
Class 1
Class 2
Class 3
Class 4
38 693 particles
18.5%
80 674 particles
38.6%
RBD 2-up-mACE2
3.03 Å (C1)
RBD 3-up-mACE2
2.89 Å (C1)
Focussed refinement
2.96 Å (C1)

Figure S5

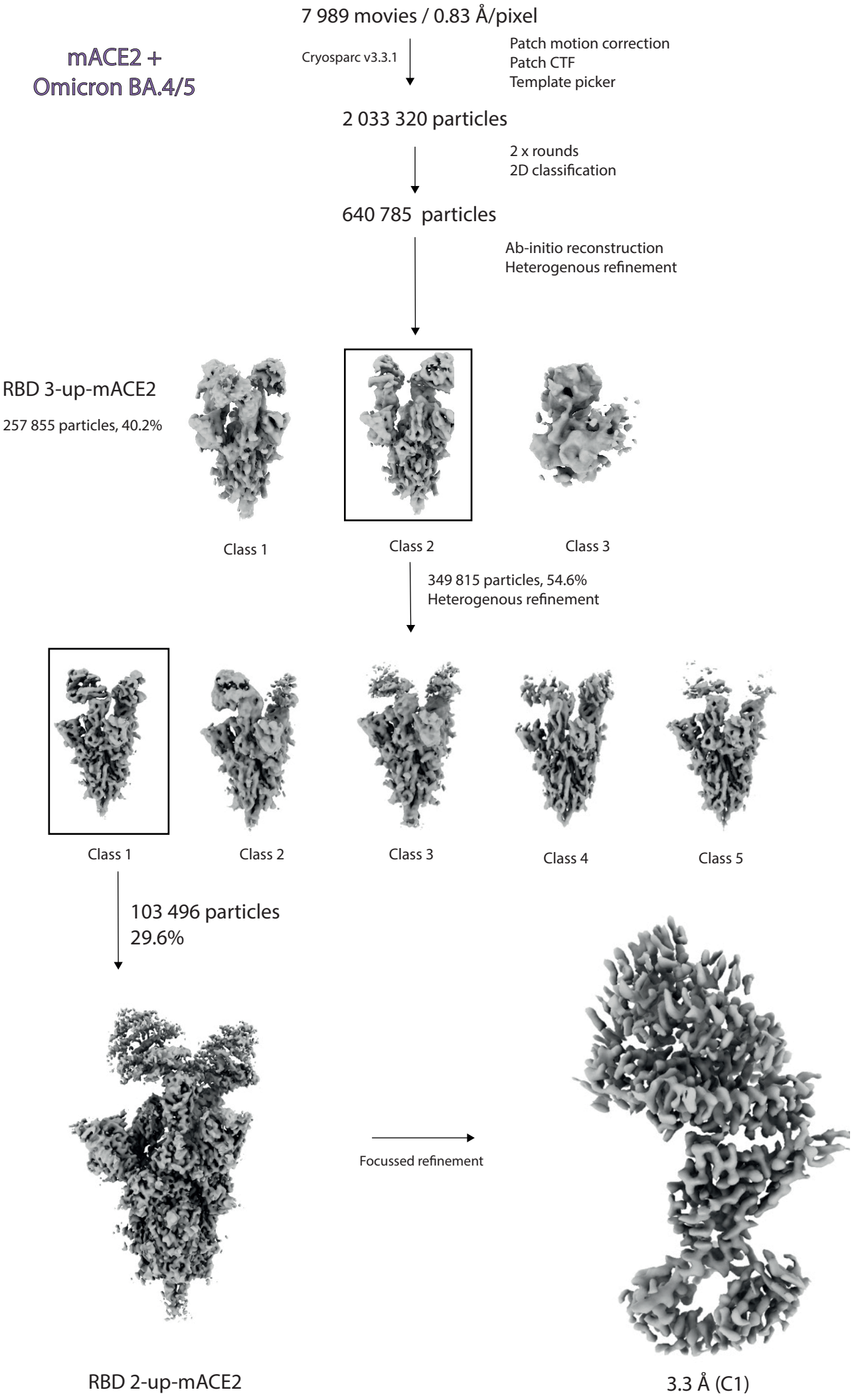
mACE2 +
Omicron BA.4/5
7 989 movies / 0.83 Å/pixel
Cryosparc v3.3.1
Patch motion correction
Patch CTF
Template picker
2 033 320 particles
2 x rounds
2D classification
640 785 particles
Ab-initio reconstruction
Heterogenous refinement
RBD 3-up-mACE2
257 855 particles, 40.2%
Class 1
Class 2
Class 3
349 815 particles, 54.6%
Heterogenous refinement
Class 1
Class 2
Class 3
Class 4
Class 5
103 496 particles
29.6%
Focussed refinement
RBD 2-up-mACE2
2.90 Å (C1)
3.3 Å (C1)

Figure S6

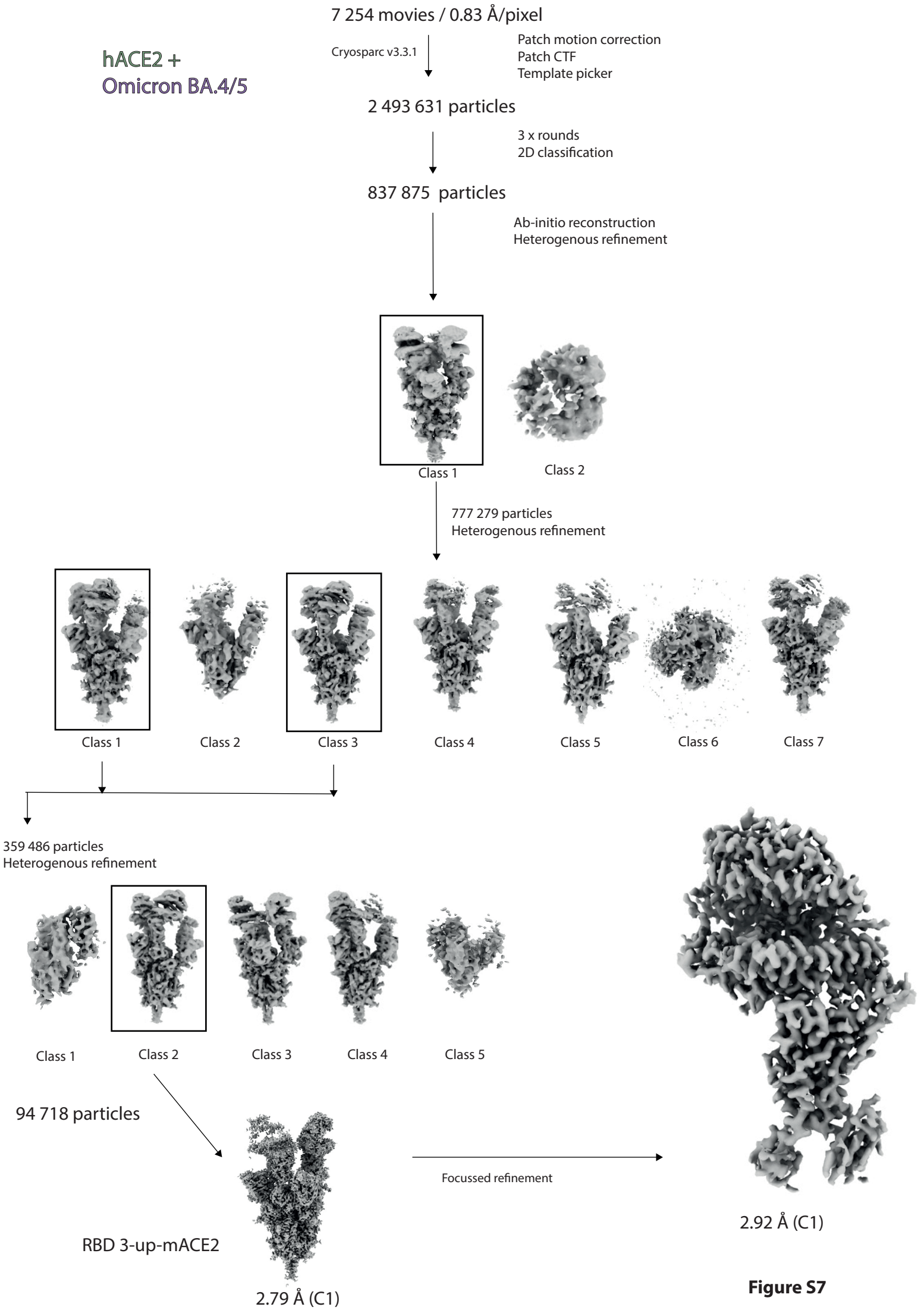
hACE2 +
Omicron BA.4/5
7 254 movies / 0.83 Å/pixel
Cryosparc v3.3.1
Patch motion correction
Patch CTF
Template picker
2 493 631 particles
3 x rounds
2D classification
837 875 particles
Ab-initio reconstruction
Heterogenous refinement
Class 1
Class 2
777 279 particles
Heterogenous refinement
Class 1
Class 2
Class 3
Class 4
Class 5
Class 6
Class 7
359 486 particles
Heterogenous refinement
Class 1
Class 2
Class 3
Class 4
Class 5
94 718 particles
RBD 3-up-mACE2
2.79 Å (C1)
Focussed refinement
2.92 Å (C1)

Figure S7

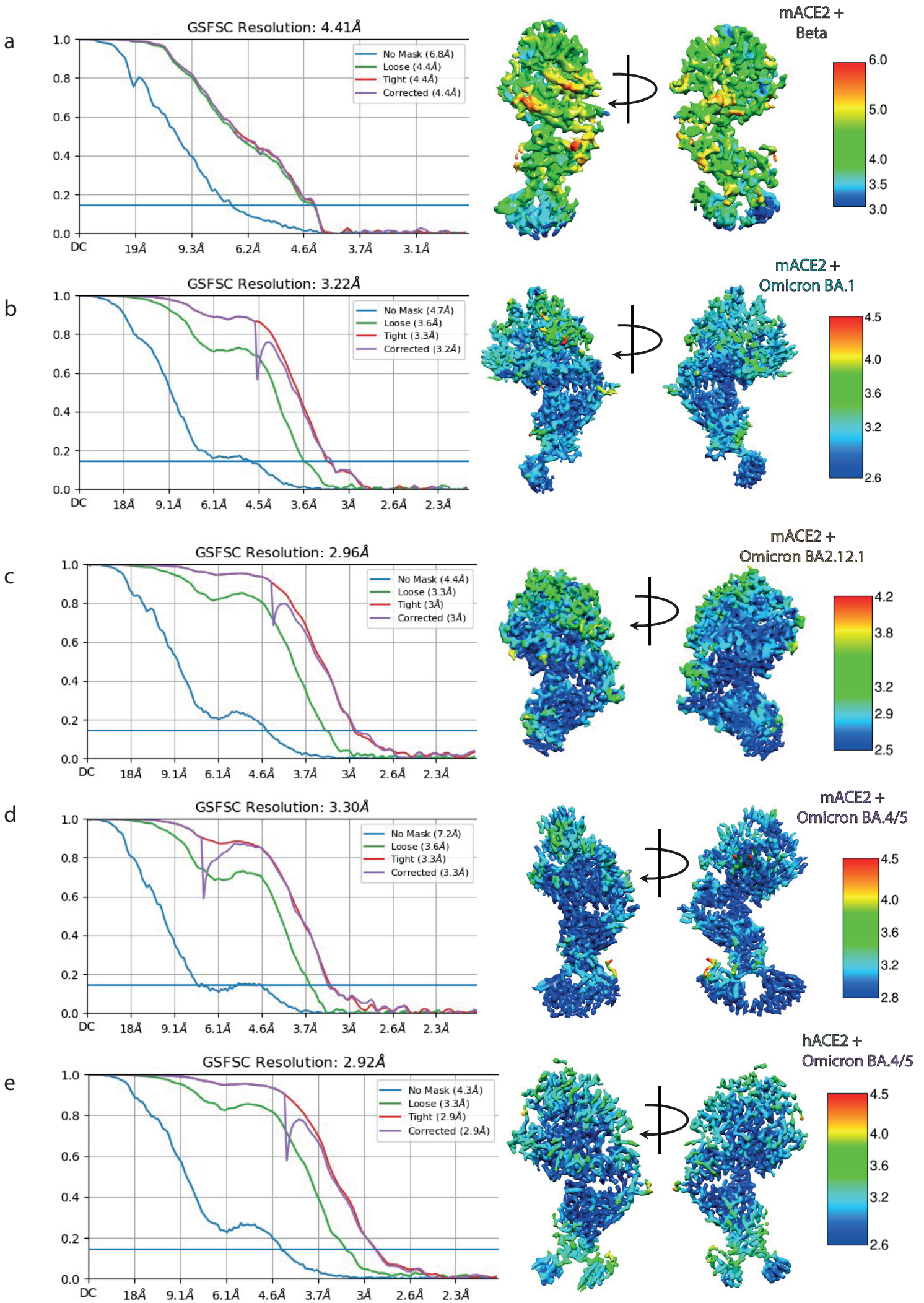
a
GSFSC Resolution: 4.41Å
No Mask (6.8Å)
Loose (4.4Å)
Tight (4.4Å)
Corrected (4.4Å)
DC 19Å 9.3Å 6.2Å 4.6Å 3.7Å 3.1Å
mACE2 + Beta
6.0 5.0 4.0 3.5 3.0
b
GSFSC Resolution: 3.22Å
No Mask (4.7Å)
Loose (3.6Å)
Tight (3.3Å)
Corrected (3.2Å)
DC 18Å 9.1Å 6.1Å 4.5Å 3.6Å 3Å 2.6Å 2.3Å
mACE2 + Omicron BA.1
4.5 4.0 3.6 3.2 2.6
c
GSFSC Resolution: 2.96Å
No Mask (4.4Å)
Loose (3.3Å)
Tight (3Å)
Corrected (3Å)
DC 18Å 9.1Å 6.1Å 4.6Å 3.7Å 3Å 2.6Å 2.3Å
mACE2 + Omicron BA2.12.1
4.2 3.8 3.2 2.9 2.5
d
GSFSC Resolution: 3.30Å
No Mask (7.2Å)
Loose (3.6Å)
Tight (3.3Å)
Corrected (3.3Å)
DC 18Å 9.1Å 6.1Å 4.6Å 3.7Å 3Å 2.6Å 2.3Å
mACE2 + Omicron BA.4/5
4.5 4.0 3.6 3.2 2.8
e
GSFSC Resolution: 2.92Å
No Mask (4.3Å)
Loose (3.3Å)
Tight (2.9Å)
Corrected (2.9Å)
DC 18Å 9.1Å 6.1Å 4.6Å 3.7Å 3Å 2.6Å 2.3Å
hACE2 + Omicron BA.4/5
4.5 4.0 3.6 3.2 2.6

Figure S8

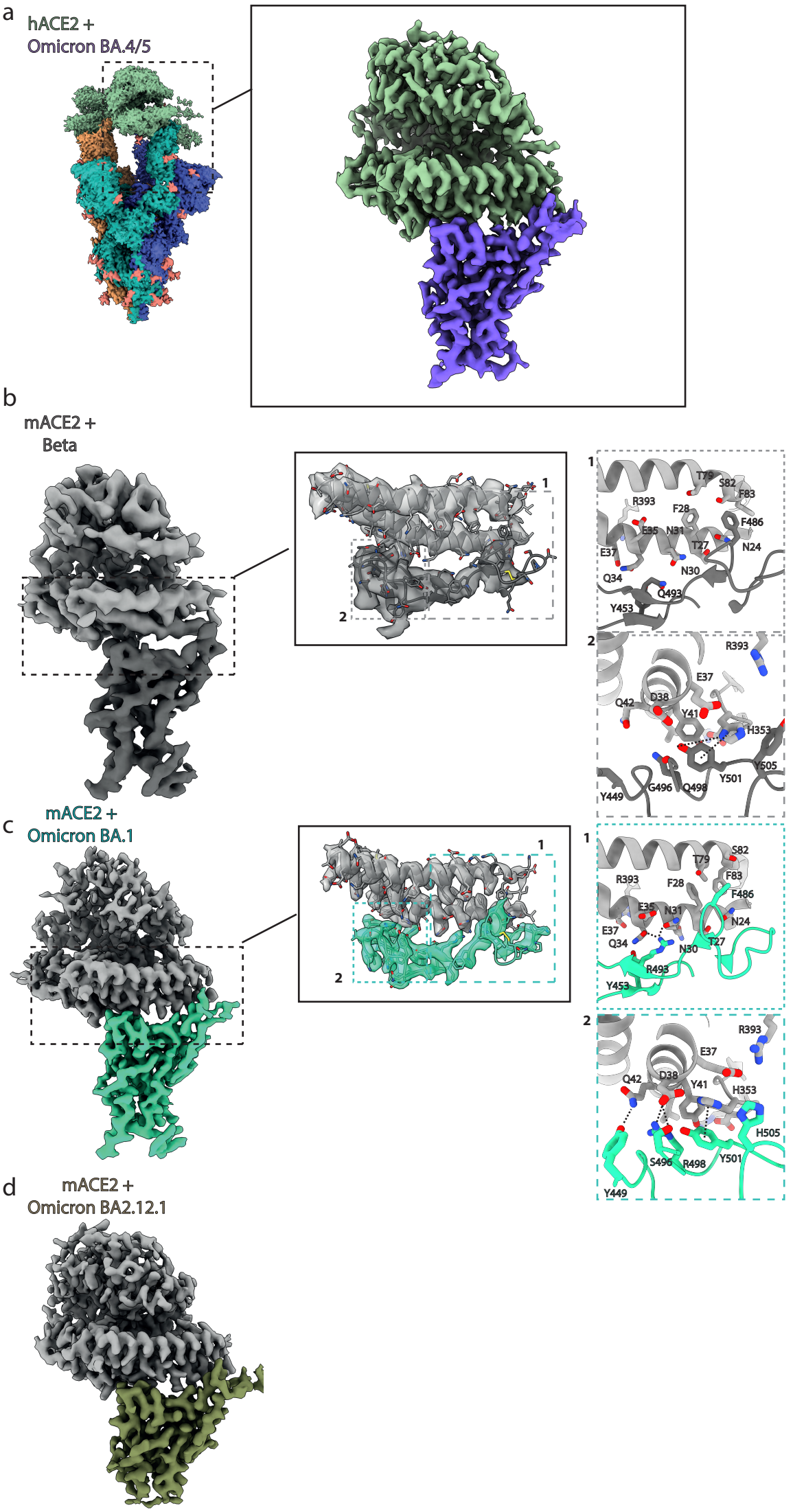
a
hACE2 +
Omicron BA.4/5
b
mACE2 +
Beta
1
2
T79
S82
F83
R393
F28
F486
E35
N31
T27
N24
E37
N30
Q34
Q493
Y453
R393
E37
Q42
D38
Y41
H353
Y505
Y501
Y449
G496
Q498
c
mACE2 +
Omicron BA.1
1
2
T79
S82
F83
R393
F28
F486
E35
N31
N24
E37
Q34
N30
T27
R493
Y453
R393
E37
Q42
D38
Y41
H353
H505
S496
R498
Y501
Y449
d
mACE2 +
Omicron BA2.12.1

Figure S9

318 **SUPPLEMENTARY FIGURE LEGENDS**

319 **Supplementary information, Fig. S1**: BLI binding assays of mACE2 and hACE2 to various
320 variants and variants of concern. **a** BLI binding assays of captured dimeric mouse or human
321 ACE2 versus various concentrations of BA.2. Data curves are colored by concentration and
322 the black line indicates the 1:1 fit of the data. **b** BLI binding curves of ACE2 at one
323 concentration of 75 nM against a panel of variants of concerns and single mutants. N501Y
324 and E484K mutations together are required for high affinity binding to mACE2 on a
325 prototypic wild-type background.

326

327 **Supplementary information, Fig. S2**: Overview of the domain architecture of selected
328 variants of concern. Mutations are shown as red lines and labelled for each variant. Specific
329 domains are highlighted: signal peptide (SP), N- terminal domain (NTD), receptor binding
330 domain (RBD), S1 and S2 domain.

331

332 **Supplementary information, Fig. S3**: Cryo-EM processing of the mACE2/Beta complex
333 **Supplementary information, Fig. S4**: Cryo-EM processing of the mACE2/BA.1 complex
334 **Supplementary information, Fig. S5**: Cryo-EM processing of the mACE2/BA.2.12.1
335 complex
336 **Supplementary information, Fig. S6**: Cryo-EM processing of the mACE2/BA.4/5 complex
337 **Supplementary information, Fig. S7**: Cryo-EM processing of the hACE2/BA.4/5 complex
338 **Supplementary information, Fig. S8**: FSC curves indicating resolutions at (FSC 0.143) and
339 final focused refined maps colored by local resolution.

340

341 **Supplementary information, Fig. S9**: Additional views of ACE2-Spike variant of concern
342 complexes. **a** Cryo-EM density of the full hACE2/BA.4/5 complexes with the inset showing
343 the focused refinement of the RBD-ACE2 interface. **b** Focused refinement of the RBD-ACE2
344 interface of the mACE2/Beta complex showing the cryo-EM density. Inset shows the zoomed
345 in view of the binding interface. Further zoomed in views of specific interaction sites of patch
346 1 and patch 2. **c** Focused refinement of the RBD-ACE2 interface of the mACE2/BA.1
347 complex showing the cryo-EM density. Inset shows the zoomed in view of the binding
348 interface. Further zoomed in views of specific interaction sites of patch 1 and patch 2. **d**
349 Focused refinement of the RBD-ACE2 interface of the mACE2/BA.2.12.1 complex showing
350 the cryo-EM density.